View metadata, citation and similar papers at core.ac.uk
brought to you by CORE
provided by Woods Hole Open Access Server

AGU100 ADVANCING EARTH AND SPACE SCIENCE

Geochemistry, Geophysics, Geosystems

RESEARCH ARTICLE
10.1029/2018GC007705

Key Points:
- Stable carbon isotopic ratios of methane in the vertical water column change because of the fractionation effect from methane dissolution
- The instantaneous Rayleigh model can be applied to accurately determine the fraction of methane dissolved from the gas to dissolved phase
- In a methane seep environment, dissolution of methane occurs rapidly after seafloor emission

Supporting Information:
- Supporting Information S1

Correspondence to:
M. Leonte,
mleonte31@gmail.com

Citation:
Leonte, M., Wang, B., Socolofsky, S. A., Mau, S., Breier, J. A., & Kessler, J. D. (2018). Using carbon isotope fractionation to constrain the extent of methane dissolution into the water column surrounding a natural hydrocarbon gas seep in the northern Gulf of Mexico. *Geochemistry, Geophysics, Geosystems*, *19*, 4459–4475. https://doi.org/10.1029/2018GC007705

Received 25 MAY 2018
Accepted 14 OCT 2018
Accepted article online 20 OCT 2018
Published online 12 NOV 2018

©2018. American Geophysical Union. All Rights Reserved.

Using Carbon Isotope Fractionation to Constrain the Extent of Methane Dissolution Into the Water Column Surrounding a Natural Hydrocarbon Gas Seep in the Northern Gulf of Mexico

M. Leonte[1], B. Wang[2], S. A. Socolofsky[3], S. Mau[4], J. A. Breier[5,6], and J. D. Kessler[1]

[1]Department of Earth and Environmental Sciences, University of Rochester, Rochester, NY, USA, [2]Department of Civil and Environmental Engineering, University of Missouri, Columbia, MO, USA, [3]Zachry Department of Civil Engineering, Texas A&M University, College Station, TX, USA, [4]MARUM-Center for Marine Environmental Sciences and Department of Geosciences, University of Bremen, Bremen, Germany, [5]School of Earth, Environmental, and Marine Sciences, University of Texas Rio Grande Valley, Port Isabel, TX, USA, [6]Applied Ocean Physics & Engineering, Woods Hole Oceanographic Institution, Woods Hole, MA, USA

Abstract A gas bubble seep located in the northern Gulf of Mexico was investigated over several days to determine whether changes in the stable carbon isotopic ratio of methane can be used as a tracer for methane dissolution through the water column. Gas bubble and water samples were collected at the seafloor and throughout the water column for isotopic ratio analysis of methane. Our results show that changes in methane isotopic ratios are consistent with laboratory experiments that measured the isotopic fractionation from methane dissolution. A Rayleigh isotope model was applied to the isotope data to determine the fraction of methane dissolved at each depth. On average, the fraction of methane dissolved surpasses 90% past an altitude of 400 m above the seafloor. Methane dissolution was also investigated using a modified version of the Texas A&M Oil spill (Outfall) Calculator (TAMOC) where changes in methane isotopic ratios could be calculated. The TAMOC model results show that dissolution depends on depth and bubble size, explaining the spread in measured isotopic ratios during our investigations. Both the Rayleigh and TAMOC models show that methane bubbles quickly dissolve following emission from the seafloor. Together, these results show that it is possible to use measurements of natural methane isotopes to constrain the extent of methane dissolution following seafloor emission.

Plain Language Summary Methane is an important greenhouse gas, and understanding emission patterns to the atmosphere is essential for assessing climate change. One of the largest methane reservoirs is found buried within ocean sediments. The natural release of this methane is predicted to increase in the future as ocean temperatures continue to warm. In ocean sediments where methane is abundant, the formation of gas bubbles can quickly transfer methane from the sediment reservoir to several hundred meters above the seafloor. However, the rate of bubble dissolution through the water column modulates to which depths methane is transported and whether methane reaches the atmosphere. Determining how far above the seafloor methane is transported is more complicated than simply detecting the presence of bubbles. Due to physical dissolution, above a certain depth, gas bubbles may no longer be transporting methane, although they continue to ascend through the water column. Since methane solubility and dissolution has been previously determined to be slightly different for different methane isotopes, here we investigate the ratio of methane stable isotopes to determine the extent of methane dissolution at different depths. By comparing the ratio of methane isotopes in gas bubbles at the seafloor to that of methane dissolved in the water column at different depths, we determine the fraction of methane that has been dissolved.

1. Introduction

Methane (CH_4), an important greenhouse gas (Ciais et al., 2013), has several different sources in oceanic environments (Reeburgh, 2007). In the northern Gulf of Mexico, subterranean stores of natural gas and oil lead to the injection of bubbles, predominantly composed of CH_4, directly into the water column, forming gas flares that reach heights of several hundred meters above the seafloor (e.g., Weber et al., 2014). Once

CH_4 is dissolved in the water phase, it can either be microbially oxidized or transported through the water column until it ultimately exchanges with the atmosphere (Mau et al., 2012). In the Gulf of Mexico, it has been debated if and how much CH_4 emanating from seafloor seeps reaches the atmosphere and whether gas bubbles play an important role in bringing CH_4 close to the surface (e.g., Hu et al., 2012; Solomon et al., 2009; Wang et al., 2016).

When a CH_4 bubble enters the water column at the seafloor, concentration gradients are established causing CH_4 to diffuse from the gas phase into the water phase and dissolved oxygen, nitrogen, argon, and carbon dioxide to diffuse from the water phase into the gas phase (McGinnis et al., 2006). By a certain depth, the dominant mol fraction within a bubble is no longer CH_4 but other gases such as oxygen, nitrogen, argon, and carbon dioxide even though CH_4 was the major constituent when the bubble was emitted from the seafloor. These bidirectional fluxes continue as a bubble ascends until equilibrium is established. Since the background concentration of dissolved methane in the open ocean is relatively low, the altitude above the seafloor to which CH_4 is transported via bubbles can be less than the depth where gas bubbles fully dissolve. Thus, the acoustic identification of bubbles in the water column is insufficient to understand the altitude of methane transport.

Here we utilize the natural stable isotopic content of CH_4 as an independent measure of the extent of bubble dissolution at different altitudes above the seafloor. Unlike biological reactions such as CH_4 oxidation where $^{12}CH_4$ reacts at a slightly faster rate than $^{13}CH_4$ (e.g., Leonte et al., 2017), our data suggest the physical dissolution of CH_4 is preferential to the $^{13}CH_4$ isotope. For most gases, the heavier isotope has a higher solubility (Jancsó, 2002) and both empirical and theoretical studies on CH_4 have confirmed the same trend (Bacsik et al., 2002; Harting et al., 1976). Since gases with higher solubility reach equilibrium between phases quicker (Garcia-Tigreros Kodovska et al., 2016; Johnson, 1999), we expect the rate of gas exchange to be faster for the heavier $^{13}CH_4$ isotope. However, dissolution is driven by two gradients, the solubility of CH_4 in the water phase and the molecular diffusion of CH_4 across the gas-liquid boundary. Molecular diffusion is faster for the lighter $^{12}CH_4$ isotope under standard laboratory conditions, potentially counterbalancing the solubility effect, but under more turbulent conditions, such as a rising bubble plume, isotopic fractionation due to molecular diffusion is diminished (Knox et al., 1992). The data presented here suggest that fractionation due to molecular diffusion is negligible during bubble dissolution. Therefore, isotopic ratios of CH_4 in both the gas and liquid phases of a bubble plume are controlled by the fractionation due to solubility and the extent of dissolution.

In the investigation presented here, gaseous and seawater samples were collected so that measurements of $\delta^{13}C\text{-}CH_4$ could be used to constrain the extent of dissolution. A remotely operated vehicle (ROV) was used to collect gas bubble and water samples surrounding a hydrocarbon gas seep atop Woolsey Mound located within lease plot Mississippi Canyon 118 in the northern Gulf of Mexico (Figures 1 and 2). Samples were collected within the rising bubble plume at the seafloor, 888 m, and at different depths within the water column (793, 686, 586, 482, 365, 245, and 122 m). At each depth, visual and acoustic instruments were used to guide the ROV so that samples could be precisely collected inside and outside the bubble flare. Gas bubble and water samples were collected and were analyzed for, among other things, the concentration and stable carbon isotopic content of methane, $\delta^{13}C\text{-}CH_4$. A complete list of the data and accompanying metadata can be found in Kessler and Leonte (2018).

The results presented here indicate that dissolved $\delta^{13}C\text{-}CH_4$ becomes lighter (more negative) closer to the surface, consistent with expectations given a rising CH_4 bubble and the preferential dissolution of the $^{13}CH_4$ isotope (Figure 1). An instantaneous product isotope model, a version of the Rayleigh isotope equation, was used to calculate the fraction of CH_4 released from the seafloor that had dissolved (Harting et al., 1976). These measurement and model results were then compared against those determined with the single bubble module in the Texas A&M Oil spill (Outfall) Calculator (TAMOC; Wang & Socolofsky, 2018). The TAMOC model independently calculated both the fraction of CH_4 dissolved as well as the changing CH_4 isotopes in the gas and dissolved phases as a bubble ascends through the water column. The extent of CH_4 dissolution and the dissolved $\delta^{13}C\text{-}CH_4$ calculated using the TAMOC model agrees with the values measured in the water column and produced from the Rayleigh isotope model when a range in bubble sizes is considered. While microbial oxidation of CH_4 did appear to be influencing the isotopic values for several samples, the short residence time of water in the bubble flare did not enable significant CH_4 oxidation in

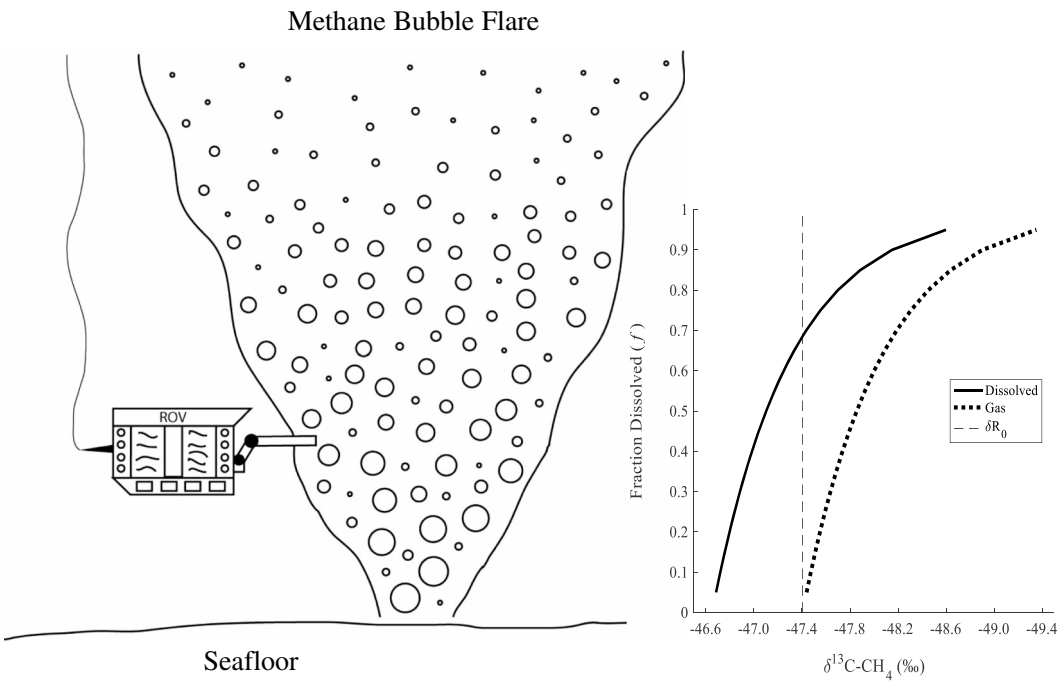

Figure 1. Schematic of a rising bubble flare and sampling operations. As bubbles rise through the water column they become smaller and less abundant due to dissolution. On the right, a plot of theoretical Rayleigh distillation curves for the dissolution of CH_4 is also included. This plot shows how $\delta^{13}C$-CH_4 values in the dissolved and gas phases change as the fraction of CH_4 dissolved since seafloor emission, *f*, increases. At the seafloor where bubbles are emitted, *f* is equal to 0, but as bubbles rise and dissolve, *f* approaches 1. Dissolved $\delta^{13}C$-CH_4 was calculated for *f* values of 0.05–0.95 using equation (1) assuming a fractionation factor of α_d=0.99932, solid line. The residual $\delta^{13}C$-CH_4 in the gas bubble was also calculated, dotted line. The initial gas $\delta^{13}C$-CH_4, δR_0, was the average gas bubble $\delta^{13}C$-CH_4 measured at the seafloor during this project, −47.41‰, dashed line. Since $^{13}CH_4$ dissolves preferentially, $\delta^{13}C$-CH_4 in the water phase is initially heavier than the starting gas, but as the bubble ascends and becomes depleted in $^{13}CH_4$, both gaseous and dissolved $\delta^{13}C$-CH_4 values become lighter.

this spatially limited region, and the dissolution isotope effect dominated. Taken together, this suggests that the assumptions made by the Rayleigh model are valid in this environment and that natural $\delta^{13}C$-CH_4 measurements inside a bubble flare can be used to calculate the fraction of gaseous CH_4 released at the seafloor that dissolved in the overlying waters (Figure 1).

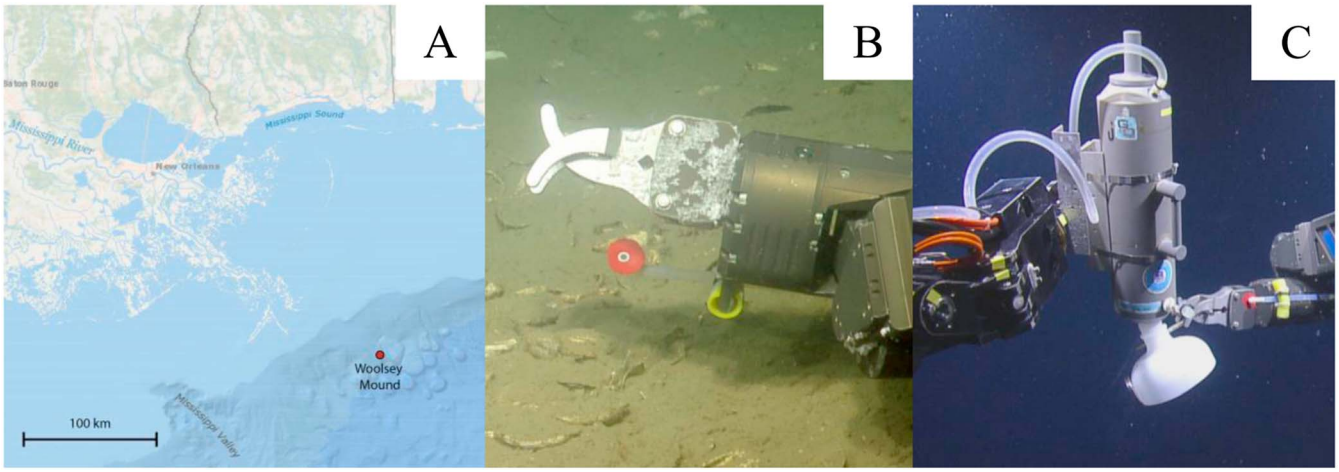

Figure 2. (a) Map of the sample site within the Northern Gulf of Mexico. (b) Image of the remotely operated vehicle sampling arm with the Suspended Particulate Rosette sampler inlet tube and red deflector shield. (c) Image of the gas bubble collection apparatus on the left and the remotely operated vehicle sampling arm on the right.

2. Materials and Methods

2.1. Sample Collection

2.1.1. ROV Sampling

Samples were collected from 12 to 20 April 2015 onboard the E/V *Nautilus*. Our study was focused on a gas seep atop Woolsey Mound (28.852150°N, 88.491830°W) which is part of lease plot Mississippi Canyon 118 in the northern Gulf of Mexico (Figure 2a). Previous studies have described the hydrographic, geophysical, geological, geochemical, and biological processes active at Woolsey Mound (e.g., Macelloni et al., 2013, 2016). Water and gas samples were collected inside and outside the natural gas bubble column at multiple depths using the ROV *Hercules* (Figure 1). Since visibility was limited to only a few meters in front of the ROV, acoustic devices were utilized to identify and track the bubble column's position, enabling sample collection at precise positions within the bubble plume. Two acoustic devices were fitted to the ROV *Hercules*, a forward-facing Kongsberg M3 Multibeam Echosounder and a bottom-facing Simrad EK80 WBT Tube. The bottom-facing sonar guided the ROV positioning on top of the bubble column, while the front-facing sonar guided the ROV laterally in the bubble column. Once the ROV was positioned in the appropriate location, water or gas sample collection was initiated. It was also possible to view the main ROV *Hercules* from the *Argus* ROV, helping to ensure that the sample collection occurred in the bubble stream at all times, validation that was especially helpful at positions where the seafloor was not visible. A total of seven dives was undertaken where water samples and/or gas bubble samples were collected. In total, 3 gas samples and 66 water samples were collected and used in the calculations described here. A more detailed description of sampling locations can be found in the supporting information.

2.1.2. Water Samples

The ROVs *Hercules* and *Argus* were used in tandem, and *Hercules* was retrofitted with the Suspended Particulate Rosette (SUPR) Sampler designed for deep-sea water sample collection (Breier et al., 2014). Briefly, the SUPR sampler is capable of collecting water samples at depths as great as 5,000 m in a wide array of oceanic settings including extreme environments such as hydrothermal vents. An inlet tube used to collect water samples was attached to the manipulator arm of the ROV, making it visible in the ROV cameras and possible to use the ROV's positioning capabilities to precisely collect samples inside and outside the bubble column. A small deflector shield was placed on the end of the inlet tube to allow water to be sampled inside the bubbly region without collecting gas bubbles (Figure 2b). A continuous pump was used to draw water through the sample tube and fill one of the designated, 2-L PerFluoroAlkoxy (PFA) plastic bottles. Each bottle was flushed with seawater a total of 5 times before filling; based on the flow rate and bottle volume, each sample was collected over a timespan of roughly 5 min. Occasionally, the position of the gas bubble column fluctuated on timescales shorter than 5 min due to variable bubble emission intensities and ocean currents. Thus, for certain samples, the ROV was repositioned during sampling to remain inside the bubble column, and occasionally, if the column moved significantly, sampling was halted, the ROV was repositioned, and the sample collection process was restarted from the beginning.

The PFA plastic bottles were designed to allow water to be transferred to other containers for gas tight storage. The PFA bottle caps had an outlet port and a second port connected to a tube that reached close to the bottom of the bottle. When the bottle was held upside down, hydrostatic pressure pushed water down and out through the outlet port while air filled the bottle from the top, thus reducing mixing between the water sample and ambient air. Once the ROV was recovered on deck, water was transferred from the PFA plastic bottles into glass vials (Wheaton) using Tygon tubing. Vials were filled from the bottom, and care was taken to prevent bubble formation within the vials. Glass vials of two sizes were used: 120 ml for CH_4 concentration analysis and 500 ml for isotopic ratio analysis. For each water sample collected using the SUPR sampler, a vial for CH_4 concentration analysis and a vial for isotopic ratio analysis were filled. The 2-L sample volume of the PFA bottles was enough to flush each vial twice before filling it. A 10-ml helium headspace was introduced into each capped vial while simultaneously removing 10 ml of water, followed by the addition of a supersaturated solution of mercuric chloride ($HgCl_2$) to preserve the samples. Using a gastight Hamilton syringe, 50 μl of $HgCl_2$ was added to the 120-ml vials and 100 μl was added to the 500-ml vials. Vials meant for CH_4 concentration analysis were stored in a temperature-controlled incubator set to 4 °C (i.e., similar to in situ temperatures) for at least 12 hr to allow for gas equilibration in the headspace before analysis onboard the ship. While prior experience indicated that 12 hr is sufficient to reach gas equilibrium, the samples were periodically shaken, both manually and due to the natural motion of the ship, to help establish equilibrium.

Samples collected for CH_4 isotopic ratio analysis were stored at room temperature and analyzed on shore at the Woods Hole Isotope Laboratories.

2.1.3. Gas Samples

Samples of gas bubbles were collected using a custom-built gas sampler made up of two plastic cylinders (modified Niskin bottles) and a funnel (Figure 2c). A primary cylinder was open at the bottom with a funnel attached underneath it to increase the surface area over which gas bubbles were collected. The primary cylinder and secondary cylinder were connected by a tube attached to the top of each cylinder. The secondary cylinder also had a drain tube attached to the bottom. Gas samples were collected by positioning the ROV within the bubble column and using the funnel to direct gas bubbles into the primary cylinder. After the primary cylinder was filled with gas, the bottom of the cylinder was closed. As the ROV ascended to be brought back on board, decreasing water pressure allowed the gas sample in the primary cylinder to expand into the secondary cylinder, driving out water through the drain tube. By the time the ROV was recovered, minimal water remained inside the secondary container. Gas samples were transferred to 120-ml glass vials capped with butyl rubber stoppers and aluminum crimp caps (Wheaton). Vials were prepared by flushing with nitrogen for several minutes before capping. A needle perforating the butyl stopper allowed the nitrogen contained inside the vial to be evacuated after the vial was flushed and capped. The seep gas sample was pulled out of the secondary cylinder using a 60-ml syringe, while a second 60-ml syringe was simultaneously used to fill the displaced volume with water, thus maintaining atmospheric pressure within the sample cylinder. Finally, the extracted gas sample was injected into the evacuated vial and the process was repeated until the vial pressure was slightly above atmospheric pressure. Gas samples were stored at room temperature until analysis at the Woods Hole Isotope Laboratories for gas composition and $\delta^{13}C\text{-}CH_4$.

2.2. Analytical Measurements

2.2.1. Dissolved Hydrocarbons Analysis

Samples were analyzed onboard the E/V *Nautilus* for dissolved concentrations of methane, ethane, propane, and n-butane using an Agilent 6850 gas chromatograph equipped with a flame ionization detector. Approximately 5 ml of the headspace gas was removed from each sample vial and used to flush and fill a 50-μl sample loop. The sample loop was connected to a two-position Valco Valve that transferred the sample gas onto a Gas-Pro capillary column (length = 15 m, inner diameter = 0.32 mm, Agilent) using a helium carrier gas. The carrier gas flow rate began at 2 ml/min and was increased to 4 ml/min after 2 min. The gas chromatograph oven temperature was set to 40 °C at the start of the run and was increased to 80 °C after 3.5 min, leading to a total run time of 5.5 min. Retention times were 0.93, 1.44, 3.10, and 5.24 min for methane, ethane, propane, and n-butane, respectively. At the start of each day, a calibration curve was generated using nitrogen as a blank and three standards (Air Liquide) containing methane, ethane, propane, and n-butane. Methane standards had concentrations of 1, 10, and 100 ppm; ethane standards were 1, 2, and 10 ppm; and propane and n-butane standards had the same concentrations of 0.5, 1, and 10 ppm. One additional standard contained only methane with a concentration of 800 ppm. Based on the calibration curves, the concentrations of gases in the vial headspace were calculated and combined with published solubility data to determine the initial dissolved concentrations of hydrocarbons in the water samples (Ben-Naim & Yaacobi, 1974; Rice et al., 1976; Umano & Nakano, 1958; Wiesenburg & Guinasso, 1979). Precision for these analyses was 1.1%, 1.0%, 2.3%, and 2.2% for methane, ethane, propane, and n-butane, respectively.

2.2.2. Methane Isotopic Ratio Analysis

Methane $\delta^{13}C$ isotopic analyses for dissolved and gaseous samples were performed at the Woods Hole Isotope Laboratories using the method described previously (Leonte et al., 2017). Briefly, vial headspace samples were preconcentrated prior to compound separation using an Agilent 6890 Gas Chromatograph. Methane gas was then converted to CO_2 using a Finnigan GCCIII combustion interface and analyzed on a Thermo Finnigan DeltaPlus XL isotope ratio mass spectrometer. Measured isotopic ratios were then converted to standard delta notation, $\delta^{13}C\text{-}CH_4$:

$$\delta^{13}C = \left[\frac{\left({}^{13}C/{}^{12}C\right)_{\text{measured}}}{\left({}^{13}C/{}^{12}C\right)_{\text{standard}}} - 1\right] \times 1000$$

Using the Pee Dee Belemnite isotope standard,

$$\left({}^{13}C/{}^{12}C\right)_{standard} = 0.0112372$$

2.2.3. Methane Isotopic Ratio Correction

The headspace technique used to prepare water samples for the analysis of $\delta^{13}C\text{-}CH_4$ partitions dissolved CH_4 in the sample vial between the gas (i.e., headspace) and liquid phase. Since the solubility of CH_4 differs between isotopes, some isotopic fractionation should occur between the dissolved CH_4 and the gaseous CH_4 in the headspace. This means that the $\delta^{13}C\text{-}CH_4$ measured in the headspace is slightly different from the $\delta^{13}C\text{-}CH_4$ dissolved in the original water sample before a headspace was inserted. Fortunately, the $\delta^{13}C\text{-}CH_4$ measured in the headspace can be corrected to the original $\delta^{13}C\text{-}CH_4$ using an isotope mass balance between dissolved and headspace CH_4.

$$\mathrm{mol}_i\delta i = \mathrm{mol}_d\delta d + \mathrm{mol}_h\delta h$$

Here i, d, and h represent the moles or $\delta^{13}C$ of CH_4 initially in the seawater sample or in the dissolved or headspace gas of the prepared sample, respectively. The value for δd was determined using the measured value of δh with the isotopic fractionation factor associated with CH_4 dissolution, α_d. This isotopic fractionation factor can be defined as the ratio of dissolution rate constants of the light isotope over the heavy isotope or the isotopic ratio of heavy to light CH_4 isotopes dissolved in water over the same ratio of isotopes in the headspace at equilibrium:

$$\alpha_d = k_L/k_H = \frac{(H/L)_d}{(H/L)_h} = \frac{\delta d + 1000}{\delta h + 1000}$$

The specific derivation of the relationship between α_d and the $\delta^{13}C\text{-}CH_4$ in the headspace and dissolved in water can be found in Leonte and Kessler (2018). For a laboratory temperature of 20 °C, α_d was measured to be 0.99938 (Harting et al., 1976). Finally, based on CH_4 concentration measurements and the partitioning of CH_4 between the dissolved phase and the headspace due to solubility (Wiesenburg & Guinasso, 1979), the isotopic ratio of CH_4 dissolved in the original water sample, δi, was calculated.

2.2.4. Gas Bubble Composition Analysis

Gas composition was determined using a Hewlett Packard 5890 Series II gas chromatograph fitted with a 6′ HayesSep-Q packed analytical column operated in constant flow mode with an He carrier gas. Aliquots of gas were introduced via a purpose-built valve system, separated by the analytical column, and detected by a thermal conductivity detector and flame ionization detector connected in series. Individual signals were recorded using HP Chemstation, and Mol % was calculated by comparing the areas of a two-point calibration curve generated by injecting different volumes of a natural gas calorimetric standard obtained from Matheson Tri Gas to the areas of the unknowns injected.

2.3. Calculating the Fraction of Methane Dissolved Using Natural Isotopic Ratios

Given that $\delta^{13}C\text{-}CH_4$ dissolves preferentially into the water column, we would expect CH_4 isotopic ratios measured in gas bubbles to be lighter than CH_4 dissolved in the water column (Harting et al., 1976) and dissolved CH_4 isotopic ratios to become lighter as bubbles rise in the water column and dissolution progresses (Figure 1). This makes the dissolution process comparable to Rayleigh distillation, a process which was originally used to describe the changing stable isotope signature of precipitation (Dansgaard, 1964). The product, in this case dissolved CH_4, is described with an instantaneous Rayleigh fractional model (Dansgaard, 1964; Hoefs, 1997), since the dissolved CH_4 does not accumulate in one parcel of water as dissolution progresses but instead is distributed vertically throughout the water column as the bubble ascends (equation (1) and Figure 1). A complete derivation of (equation (1)) is provided in the supporting information.

$$\delta X = \frac{(\delta R_0 + 1,000)}{\alpha_d} * (1 - f)^{\left(1/\alpha_d - 1\right)} - 1,000 \tag{1}$$

Here δX represents the isotopic ratio of CH_4 being dissolved into the water column, δR_0 is the initial isotopic ratio of CH_4 inside a gas bubble released at the seafloor, α_d is the temperature dependent fractionation factor associated with CH_4 dissolution, and f is the fraction of CH_4 inside the gas bubble that has been dissolved

since the gas bubble entered the water column. The isotopic ratios in this equation are in delta notation based on the conversion described in section 2.2.2. The fractionation factor associated with dissolution, α_d, is defined as the ratio of dissolution rate constants of the light isotope over the heavy isotope.

It would be incorrect to calculate *f* based on a change in bubble size, since bubble size is not conservative (McGinnis et al., 2006); rather, the total moles of CH_4 within the bubble is necessary to calculate *f*. Collecting gas samples in the deep ocean that enables the total moles of CH_4 to be determined requires unconventional sampling equipment to maintain in situ pressure (e.g., Seewald et al., 2002), thus making direct determinations of *f* challenging. However, collecting seawater samples for the analysis of dissolved δ^{13}C-CH_4 can be accomplished with more standard oceanographic techniques involving Niskin bottles (e.g., Leonte et al., 2017). Thus, we rearrange equation (1), so that *f* can be calculated from values of dissolved δ^{13}C-CH_4, more easily collected with standard techniques (equation (2)).

$$f = 1 - \left[\frac{(\delta X + 1,000)}{(\delta R_0 + 1,000)} * \alpha_d\right]^{\alpha_d/(1-\alpha_d)} \tag{2}$$

2.4. Seep Bubble Modeling of Fraction Dissolved and Isotopic Fractionation

We simulate the dissolution of natural gas bubbles in the water column using an approach similar to McGinnis et al. (2006). The model used in this study is the single bubble module in TAMOC, which has been validated to numerous data sets for bubble and plume behavior (Gros et al., 2016, 2017). This model computes the equations of state of real gas mixtures and the physical properties of the bubbles (shape, rise velocity, etc.) to solve a mass transfer equation for each component in a bubble. We applied the model to calculate the dissolution of CH_4 (both ^{12}C and ^{13}C) from bubbles during their ascent from the seafloor and thereby obtained predicted profiles of the fraction of CH_4 dissolved and dissolved δ^{13}C-CH_4 within the seep bubble flare.

The ambient water column properties (pressure, temperature, and salinity) used in the model were measured by a CTD (SeaBird SBE 49 FastCAT) mounted on the ROV. Ambient currents were recorded by an Acoustic Doppler Current Profiler at a nearby National Data Buoy Center station (Station # 42883, 28°51′0″N, 88°28′18″W, located 1.98 km from the seep source). Dissolved gases were estimated by equilibrium with the atmosphere and corrected for seawater compressibility (O_2, N_2, Ar, and CO_2 were included in the ambient profile). The initial conditions required to run the model include the gas composition of bubbles and the bubble size distribution. Gas composition was measured from the collected samples, and the complete gas composition of the bubbles is provided in Table 1 and can be found in Kessler and Leonte (2018). The gas samples were collected at the seafloor in dives H1405 and H1406, along with a 200-m altitude sample in dive H1407. The bubble size distribution at the seafloor was measured using a stereoscopic imaging system (Wang & Socolofsky, 2015), following the same procedure as in the Gulf Integrated Spill Response Consortium research cruise G07 (Wang et al., 2016). The TAMOC model simulated 1,000 randomly generated bubbles based on a lognormal distribution that best fit the water column bubble size measurements (Figure 3). For dives H1405 and H1406, bubble release was simulated by the model at the seafloor, 890-m depth. However, during dive H1407, gas composition was measured 200 m above the seafloor or at 690-m depth, and therefore, the TAMOC model was initialized at this depth when simulating dive H1407. Because we could not observe the complete bubble size distribution at this depth, we averaged the size distributions predicted by the TAMOC model for dives H1405 and H1406 at 200-m altitude to obtain the initial bubble size distribution in H1407. The effect of clathrate hydrate formation on dissolution rate was also considered in the model; we applied an algorithm for hydrate formation time calibrated to observations in Rehder et al. (2009) and validated to both the GISR G07 field data (Wang et al., 2016) and the laboratory experiment described in Warzinski et al. (2014). Although the formation and dissociation of gas hydrate shells surrounding gas bubbles can influence dissolution rate, it does not appear to fractionate CH_4 isotopes (Lapham et al., 2012). Two mass transfer rates were used in our model to distinguish the different mechanisms of bubble dissolution: clean bubble dissolution before hydrate formation and dirty bubble dissolution after hydrate formation, where clean and dirty bubble mass transfer coefficients were determined following Clift et al. (1978). The rise time to 200-m altitude (690-m depth) is several minutes, longer than typical hydrate formation times in our algorithm; hence, we also set the hydrate formation time to zero for H1407.

Table 1
Gas Bubble Composition and δ^{13}C-CH_4 Measured for Gas Bubble Samples Collected on Three Separate Dives

Dive	Altitude (m)	Depth (m)	Sample ID	$\delta^{13}CH_4$ (‰)	Methane (mole %)	Nitrogen (mole %)	Carbon dioxide (mole %)	Ethane (mole %)	Propane (mole %)	Isobutane (mole %)	n-butane (mole %)
H1405	0	888	G1	−47.06	68.37	18.80	1.89	2.42	0.87	0.17	0.34
H1406	0	888	G2	−47.75	70.26	15.99	2.78	4.02	3.25	0.74	0.55
H1407	202	686	G3	−47.10	67.57	22.85	0.37	0.94	0.33	0.20	0.07

We treated $^{12}CH_4$ and $^{13}CH_4$ as two different components of the gas mixture, each having different, yet proportional, dissolution rates, due to the isotope fractionation from CH_4 dissolution. The isotopic fractionation of CH_4 during dissolution can be caused by two factors: the difference in solubility between CH_4 isotopes and the differences in the rates of molecular diffusion of the $^{12}CH_4$ and $^{13}CH_4$ isotopes. Solubility is slightly preferential toward the heavier, $^{13}CH_4$, isotope with a fractionation factor of $\alpha_d = 0.99938 \pm 0.00005$ at 20 °C (Harting et al., 1976). Molecular diffusion is preferential toward the lighter $^{12}CH_4$ isotope, and the magnitude of fractionation is $\alpha_k = 1.0008 \pm 0.0002$ at 20 °C (Knox et al., 1992). The net effect of these two processes determines the isotopic effect on CH_4 during dissolution. However, when incorporating these effects into the TAMOC model, which fully resolves bubble dissolution, bubble turbulence causes the molecular diffusion effect to become negligible compared to fractionation due to solubility and was therefore excluded from the model calculations. In the TAMOC model, the rate of mass transfer is written as follows:

$$\frac{dm}{dt} = -kA(C_s - C_a)$$

where k is the mass transfer coefficient (m/s), A is the surface area of bubbles (m^2), C_s is the concentration of CH_4 that would be dissolved in water if the water and bubble phases were at equilibrium (kg/m^3), and C_a is the measured concentration of CH_4 dissolved in the water column (kg/m^3). In the model C_a is set to 0 since C_s values are roughly 62.5 (mmol/L) at 400-m depth and increase linearly with depth, while C_a measurements were only as high as 95.7 (μmol/L). Hence, the mass transfer equation is simplified to

$$\frac{dm}{dt} = -kAC_s$$

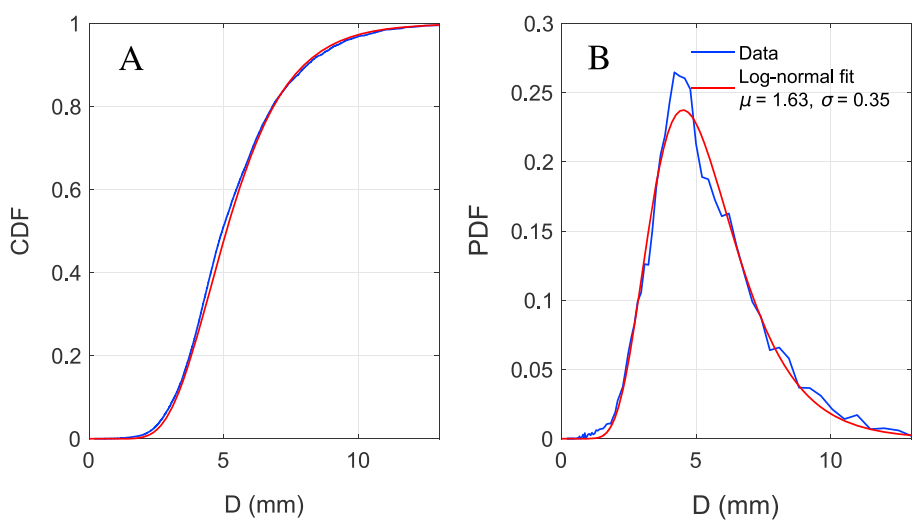

Figure 3. (a) Cumulative distribution function, CDF, and (b) probability distribution function, PDF, of bubble sizes (D, mm) considered in this study. The blue line shows measured bubble sizes from this study, while the red line is a lognormal fit to the measured data used in the TAMOC model. TAMOC = Texas A&M Oil spill (Outfall) Calculator.

The fractionation effect due to solubility is reflected by C_s, while fractionation due to molecular diffusion is reflected by k. In the TAMOC model, the mass transfer coefficient, k, is a function of both molecular and turbulent diffusion across the boundary of the bubble surface. Water column measurements suggest that turbulent diffusivity is 2 orders of magnitude greater than molecular diffusivity for bubbles with a hydrate shell and 3 orders of magnitude greater for bubbles without a hydrate shell (Wang et al., 2016). Therefore, the magnitude of fractionation due to molecular diffusion is expected to be at most 1% of that caused by solubility and was excluded from the TAMOC model calculations. The authors that originally measured the fractionation factor due to molecular diffusion also noted that turbulence would diminish this fractionation effect to such an extent that in a bubble plume it would be negligible (Knox et al., 1992).

Thus, the fractionation factor used to model the entire dissolution process was simply the fractionation factor measured due to solubility effects, α_d (Harting et al., 1976). Although the experiments measuring α_d were conducted only at temperatures of 20, 50, and 80 °C, theoretical studies on isotope effects for CH_4 dissolution have determined a linear relationship that exists between α_d and temperature, allowing us to extrapolate α_d down to in situ temperatures (Bacsik et al., 2002). In this study, we used a constant value of α_d, calculated by extrapolating laboratory data to a temperature of 7.0 °C, α_d=0.99932. A temperature of 7.0 °C was chosen since this is the average in situ temperature of samples collected from the seafloor to an altitude of 406 m, over which a large proportion of dissolution occurred. The uncertainty added by assuming a constant value of α_d is small compared to other uncertainties caused by natural variabilities, such as bubble size (see section 4.2). The relative difference between the α_d value calculated at 7.0 °C and those calculated for the lowest temperature measured at the seafloor (5.4 °C) and the highest temperature measured at 406-m altitude (8.8 °C) is only 1.1% and 1.3%, respectively. Using the model, we calculated the individual mass flux of $^{12}CH_4$ and $^{13}CH_4$ dissolving into the water from the bubbles at 5-m depth intervals. The first mass flux was calculated at an altitude of 2.5 m, or 887.5-m depth, considering that the TAMOC model was prescribed a seafloor depth of 890 m. The ratio of $^{12}CH_4$ and $^{13}CH_4$ in both the dissolved and gaseous phase calculated at each altitude was converted to delta notation, $\delta^{13}C$-CH_4, using the equation in section 2.2.2.

3. Results

All data and descriptions of the analyses from these experiments are available through the Gulf of Mexico Research Initiative Information & Data Cooperative (Kessler & Leonte, 2018; Leonte & Kessler, 2018; Wang & Socolofsky, 2018).

3.1. Water Samples

Analyses of dissolved CH_4 concentration (Figure 4a) show great variability which is consistent with our observations of the rapidly changing bubble flare position and intensity within the water column. For most dives, samples were collected along transects that lined up with the width and length of the acoustically detected bubble flare, but proximity of bubbles in relation to where water samples were collected was a poor predictor of CH_4 concentrations. Samples that were collected close to each other did not always have similar concentrations. For example, samples W22 and W24 were collected 3 m apart from each other during dive H1404, yet concentrations differed by 2 orders of magnitude. Although CH_4 concentrations generally increased with depth, the highest concentration measured was not observed at the seafloor but rather 100 m above the seafloor. Samples that were collected in the same location one after the other also showed concentration differences, such as samples W1 and W2, where the concentration of the latter was nearly 3 times as large as the former. Measured CH_4 concentrations also varied with time. In dive H1402, samples W11 and W19 were collected in the same location but separated by 1.5 hr, during which time-dissolved concentrations changed by 2 orders of magnitude. Furthermore, both dives H1404 and H1407 collected samples roughly 300 m above the seafloor, yet the samples from dive H1407, collected 3 days after dive H1404, showed consistently lower CH_4 concentrations. Measurements from this research cruise show how variability in bubble column position and intensity contributes toward great variability in the magnitude and distribution of CH_4 concentrations at an instantaneous point.

Isotopic measurements of dissolved CH_4 (Figure 4b) were more consistent both spatially and temporally compared to dissolved CH_4 concentration measurements. Despite a few outliers, measurements collected from the same depth showed relatively similar $\delta^{13}C$-CH_4 values, and the data set as a whole followed a

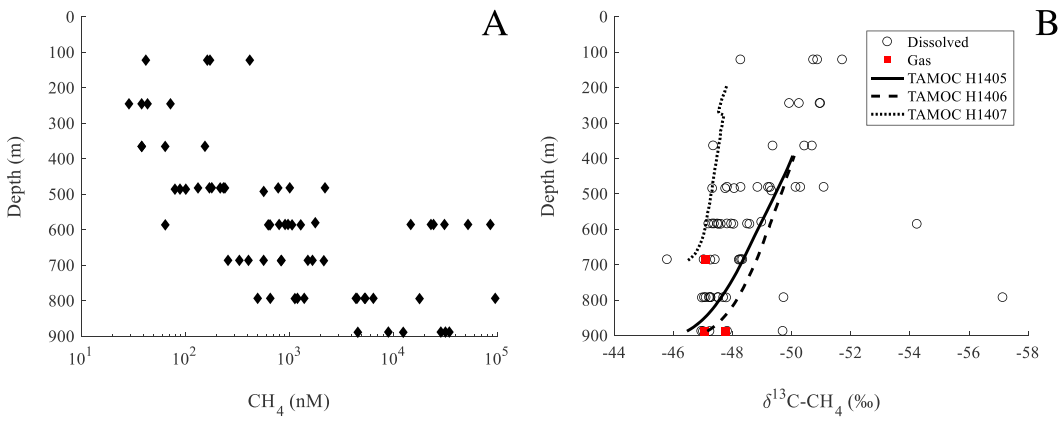

Figure 4. Measurements of dissolved CH_4 concentration (a), alongside $\delta^{13}C$-CH_4 and TAMOC model results (b) versus depth. Dissolved CH_4 concentration data show large variability over several orders of magnitude, with the highest values closest to the seafloor. The values of $\delta^{13}C$-CH_4 also show a spread for each depth sampled and a trend toward lighter values closer to the surface. TAMOC model results represent the average expected value of $\delta^{13}C$-CH_4 dissolved in the water column at any given depth. TAMOC = Texas A&M Oil spill (Outfall) Calculator.

trend toward lighter values closer to the surface. The instantaneous product model predicts that dissolved $\delta^{13}C$-CH_4 would progressively become lighter closer to the surface as more methane dissolves (Figure 1), which is an apparent trend in our measurements (Figure 4b). $\delta^{13}C$-CH_4 values were also more consistent across time. For example, samples collected consecutively at the seafloor during dive H1401, W1 and W2, showed similar values of dissolved $\delta^{13}C$-CH_4, −47.24‰ and −47.02‰, respectively, despite very different CH_4 concentrations. Samples were collected at an altitude of 300 m above the seafloor for dives H1404 and H1407. Despite the dives being 3 days apart, most isotopic values were within 2‰ of each other. These observations suggest that isotopic values of dissolved CH_4 were less affected by changes in bubble column position and intensity over time than dissolved CH_4 concentration. Also, since the seawater samples were collected within or adjacent to a rising bubble flare, the measured dissolved concentrations of CH_4 were often greater than 2 orders of magnitude above background concentrations (1–10 nM; Brooks, 1975; Hu et al., 2012; Kessler et al., 2011; Solomon et al., 2009; Yvon-Lewis et al., 2011), causing mixing with background waters to have an insignificant influence on our isotopic measurements.

3.2. Gas Samples

Gas bubble samples were analyzed for nitrogen, carbon dioxide, and hydrocarbons including methane, ethane, propane, isobutane, and n-butane. The stable carbon isotopic content of CH_4 ($\delta^{13}C$-CH_4) in the gas bubbles was also determined. Gas samples were mostly composed of CH_4 followed by nitrogen, with carbon dioxide, ethane, propane, and butane contributing relatively small and variable amounts. Gas samples, G1 and G2, were collected on dives H1405 and H1406, respectively, and separated by roughly 6 hr. The 0.7‰ difference between the two samples shows the relatively small variation of $\delta^{13}C$-CH_4 for CH_4 emitted from the seep over short timescales. Comparing gas sample G2 with values of dissolved $\delta^{13}C$-CH_4 collected at 406-m altitude during the same dive shows that dissolved CH_4 became lighter as bubbles ascended through the water column. The only gas sample collected above the seafloor was sample G3, during dive H1407, 202 m above the seafloor. Table 1 shows a summary of gas bubble composition along with $\delta^{13}C$-CH_4 isotopic values.

3.3. Computing the Fraction of CH_4 Dissolved Using the Instantaneous Product Rayleigh Model

Equation (2) was used to calculate *f*, the fraction of gaseous CH_4 that had dissolved based on measured values of $\delta^{13}C$-CH_4. Table 2 shows the average and standard deviation of *f* calculated for samples collected at the same depth, and Figure 6b shows a plot of the calculated *f* values for each sample against depth. At any given depth, there is a spread in *f* values driven by the spread in dissolved $\delta^{13}C$-CH_4 isotopic values, which may be driven by the heterogeneous spatial distribution of bubble sizes as discussed below. The data presented in Figure 6 and Table 2 demonstrate that dissolution is rapid immediately above the seafloor and that *f* approaches 1 as bubbles rise through the water column. Near the seafloor, (888-m depth) *f* values range

Table 2
Average and Standard Deviation of f, Fraction Dissolved, Calculated Using the Instantaneous Product Rayleigh Model for Each Depth Sampled Throughout the Cruise

Altitude (m)	Depth (m)	*f* value	*f* standard deviation
766	122	0.975	0.047
643	245	0.996	0.003
523	365	0.895	0.195
406	482	0.904	0.125
303	585	0.782	0.161
202	686	0.736	0.228
95	793	0.633	0.230
0	888	0.582	0.311

from 0.263 to 0.990 with an average of 0.582, meaning that more than half the CH_4 coming out of the seep is dissolved within a few meters of the seafloor. Furthermore, average *f* values indicate that CH_4 dissolution surpasses 90% by an altitude close to 400 m above the seafloor.

3.4. TAMOC Model Results

Simulations using the TAMOC model also showed aggressive dissolution of bubbles within the water column. The TAMOC model was initialized based on measured gas bubble composition and bubble size distribution, as described above, and used this data to calculate the mass of CH_4 in gas form, the flux of CH_4 from the gas into the water phase, as well as the δ^{13}C-CH_4 being dissolved and the δ^{13}C-CH_4 in the remaining gas at 5-m increments as bubbles rose vertically through the water column. Since *f* is defined as the fraction of CH_4 gas dissolved since bubble emission (section 2.3), *f* was calculated based on the ratio of CH_4 mass remaining in gas form (m_z) at any given depth to the initial mass of CH_4 in gas form at the seafloor (m_0):

$$f = 1 - \frac{m_z}{m_0} \tag{3}$$

In the TAMOC model, the seafloor was set at a depth of 890 m, and since bubbles were initialized at the seafloor, the corresponding *f* value was 0 at the seafloor, Figure 6b. Simulations where gas bubble data were collected at the seafloor, dives H1405 and H1406, showed that *f* surpassed 0.1 only 5 m above the seafloor and was greater than 0.5 at an altitude of 30 and 35 m above the seafloor for dives H1405 and H1406, respectively. Furthermore, *f* values greater than 0.9 were found 130 and 160 m above the seafloor for dives H1405 and H1406, respectively. Model results for dive H1407 showed a slower change in *f* with respect to depth. It is important to note that this dive was initialized 200 m above the seafloor, whereby a majority of bubble dissolution had already occurred. For dive H1407, *f* values surpassed 0.1, 0.5, and 0.9 as bubbles rose 15, 85, and 390 m above where the model run was initialized.

Results from the TAMOC model showed good agreement with measured water column data. Figure 4b shows a comparison between dissolved CH_4 isotopic ratios calculated by the TAMOC model and those measured from water samples. Although water samples were collected on different days and at different depths depending on the dive, dissolved δ^{13}C-CH_4 values calculated by the TAMOC model were within the natural variability of measured δ^{13}C-CH_4 values. Due to similarities in measurements of gas composition and gas bubble δ^{13}C-CH_4 from samples collected during dives H1405 and H1406, the dissolved δ^{13}C-CH_4 values calculated by the TAMOC model for these two dives were similar. Calculated dissolved δ^{13}C-CH_4 values for dive H1407 matched only the heaviest δ^{13}C-CH_4 water column measurements. This is because gas bubble δ^{13}C-CH_4 is expected to become lighter as bubbles rise through the water column, yet the measured gas bubble δ^{13}C-CH_4 from dive H1407, sample G3, collected 202 m above the seafloor, was similar in value to samples collected at the seafloor; Table 1. This is likely due to temporal variations in δ^{13}C-CH_4 of seep emissions.

Dive H1406 is ideal for comparing measured data to the TAMOC model since we collected gas bubbles and water samples at the seafloor, along with additional water samples at 406-m altitude (Figure 5). In this dive, at the seafloor, measured gas bubble δ^{13}C-CH_4 was −47.75‰ and dissolved δ^{13}C-CH_4 was −46.96‰. The TAMOC model was prescribed a starting gas δ^{13}C-CH_4 of −47.75‰ at the seafloor and predicted a dissolved δ^{13}C-CH_4 of −47.14‰ 2.5 m above the seafloor, similar to our water column measurement of −46.96‰. The TAMOC model produced values for dissolved δ^{13}C-CH_4 that were within the natural variation of measured values; at 406-m altitude, dissolved δ^{13}C-CH_4 measurements varied from −51.01‰ to −47.83‰ and the TAMOC model predicted a dissolved δ^{13}C-CH_4 value of −49.72‰ at an altitude of 407.5 m, well within the range of measured values.

Although we did not collect dissolved CH_4 samples during dive H1405, the TAMOC model results for this dive are very similar to those for dive H1406, and as Figure 4b shows, the model results also match measured data

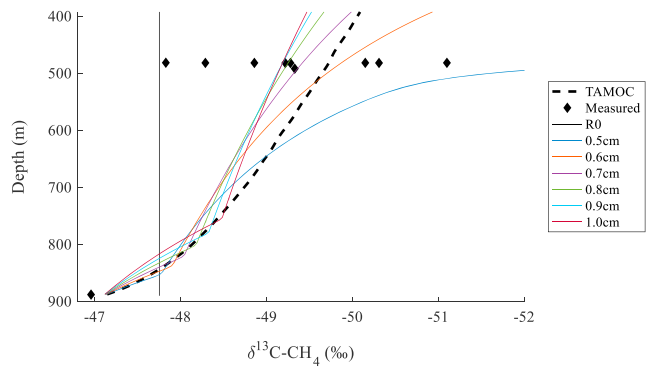

Figure 5. Comparison of the TAMOC model to measured data from dive H1406. The solid black line shows the measured initial gas bubble δ^{13}C-CH$_4$ isotopic value, −47.75‰, and the black diamonds show measured dissolved δ^{13}C-CH$_4$ isotopic values at the seafloor and at an altitude of 406 m above the seafloor (482-m depth). The black dashed line shows results from the TAMOC model using a distribution of bubble sizes based on in situ observations. All other lines have a specific bubble size prescribed at the seafloor. Bubble sizes less than 0.5 cm at the seafloor appear to lose their CH$_4$ prior to reaching an altitude of 406 m above the seafloor (482-m depth) and are not included in this figure. TAMOC = Texas A&M Oil spill (Outfall) Calculator.

from different dives collected on different days. Model results for dive H1407 only seem to match the heaviest measured isotopic values. At greater altitudes, we expect the gas bubble δ^{13}C-CH$_4$ values to be lighter than at the seafloor due to isotopic fractionation. However, the gas bubble sample collected at 202-m altitude had a δ^{13}C-CH$_4$ value that was similar or heavier than samples at the seafloor, therefore pushing the calculated δ^{13}C-CH$_4$ of dissolved CH$_4$ toward heavier values as well.

4. Discussion

4.1. Comparison of Instantaneous Product Rayleigh Model to the TAMOC Model

Two intercomparison tests were conducted to validate the use of the Instantaneous Product Rayleigh Model (equations (1) and (2)). First, we determined whether the Instantaneous Product Rayleigh Model and the TAMOC model were able to generate similar results. The Instantaneous Product Rayleigh Model predicted lighter dissolved δ^{13}C-CH$_4$ as f increased (Figure 1), and TAMOC model results showed the same relationship between dissolved δ^{13}C-CH$_4$ and f. The two models were compared by assessing the similarity in dissolved δ^{13}C-CH$_4$ values calculated by both models as a function of f (Figure 6a). As described above, the TAMOC model calculated f and δ^{13}C-CH$_4$ at 5-m increments through the vertical water column. The f values calculated by the TAMOC model simulating dive H1406 were inserted into equation (1) to determine their corresponding δ^{13}C-CH$_4$ values produced from the Instantaneous Product Rayleigh Model. Plotting the dissolved δ^{13}C-CH$_4$ calculated by both models based on the same values of f (Figure 6a) showed good agreement. Dissolved δ^{13}C-CH$_4$ calculated by the two models differed by less than 0.1‰ for f values ranging from 0 to 0.966. As f increased further, the δ^{13}C-CH$_4$ values calculated by the two models started to diverge, exceeding a 0.5‰ difference when f reached 0.995. Since f also corresponds to a certain depth in the TAMOC model, f values of 0.966 and 0.995 correspond to altitudes of 290 and 490 m above the seafloor, respectively. This comparison shows that the Instantaneous Product

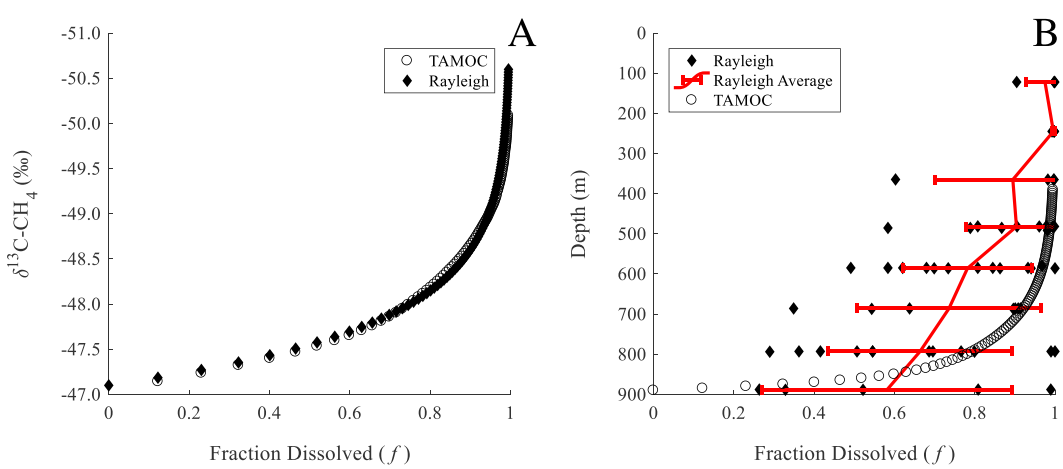

Figure 6. (a) Comparison of the TAMOC model and the instantaneous product Rayleigh model. Based on gas bubble data collected on dive H1406, the TAMOC model calculated a value for the fraction of CH$_4$ dissolved, f, and dissolved δ^{13}C-CH$_4$ at 5-m increments as bubbles rose through the water column, open circles. The f values calculated by the TAMOC model were used in the instantaneous product Rayleigh model to also calculate dissolved δ^{13}C-CH$_4$, black diamonds. The two models predicted dissolved δ^{13}C-CH$_4$ within 0.1‰ until f reached 0.966, corresponding to an altitude of 290 m or depth of 600 m in the TAMOC model. (b) Plot of f values calculated using the measured data and equation (2) and plotted as a function of depth. For this calculation, δR_0 is the average δ^{13}C-CH$_4$ in gas form collected at the seafloor during dives H1405 and H1406. The value for the fractionation factor is the same as the one used in the TAMOC model $\alpha_d = 0.99932$. The red line shows the average and standard deviation of f values calculated at the same depth; Table 2. The open circles show the same TAMOC model data as in Figure 6a but plotted against depth rather than δ^{13}C-CH$_4$. TAMOC = Texas A&M Oil spill (Outfall) Calculator.

Rayleigh Model shows agreement with the TAMOC model within the analytical uncertainty of the measurements of dissolved δ^{13}C-CH_4.

After our first test helped to validate the use of the Instantaneous Product Rayleigh Model, our second test used the Instantaneous Product Rayleigh Model to calculate *f* from our measured data and compared it to the *f* values determined with the TAMOC model (Figure 6b). The TAMOC model provides an average value of *f* based on a homogenous spatial distribution of the measured bubble sizes, while our measured data likely display how water parcels were impacted by spatial heterogeneities of bubble sizes as described in the next section. Nonetheless, when averaging the values of *f* determined from our measurements and the Instantaneous Product Rayleigh Model, we receive a profile of *f* similar to that produced from the TAMOC model (Figure 6b).

4.2. Dissolution Based on Bubble Size

Measurements of dissolved δ^{13}C-CH_4 at any given depth show a spread in isotopic ratios (Figure 4b) and although TAMOC model calculations of dissolved δ^{13}C-CH_4 initiated with a distribution of bubble sizes based on in situ observations fit within measured values (Figure 5, black dashed line), the measured values display more variation. The TAMOC model, initialized based on bubble size distribution measurements conducted at the seafloor, calculates one average value of δ^{13}C-CH_4 being dissolved in the water column at any given depth. However, this average value represents the full distribution of bubble sizes present, and in a gas seep environment, the bubble size distribution emitted at the seafloor may distribute in a spatially heterogeneous way during ascent. Since smaller bubbles have a greater surface area to volume ratio, CH_4 dissolves at a relatively faster rate compared to larger bubbles (McGinnis et al., 2006). And since the extent of dissolution determines *f*, a water parcel impacted by a greater proportion of smaller bubbles will show higher values of *f* and lighter (more negative) δ^{13}C-CH_4 compared to a water parcel impacted by larger bubbles.

In order to test the significance of bubble size on dissolved δ^{13}C-CH_4, we ran several simulations using the TAMOC model where the initial bubble size at the seafloor was prescribed different fixed values. Figure 5 shows several TAMOC model simulations where the starting bubble diameter was fixed, alongside TAMOC model results presented in section 3.4 that used the measured bubble size distribution from Figure 3. All runs were initialized using measured gas composition and δ^{13}C-CH_4 collected from dive H1406 and assumed that gaseous δ^{13}C-CH_4 emitted from the seep did not change considerably over the duration of sample collection, an assumption supported by our measurements (Table 1). Since changes in δ^{13}C-CH_4 are correlated to the extent of bubble dissolution, *f*, these results show how smaller bubbles dissolved more quickly than larger bubbles and are less likely to transport CH_4 as far vertically through the water column. An interesting suggestion from this exercise is that measured values of dissolved δ^{13}C-CH_4 might be useful for estimating the initial bubble size at the seafloor, since at any given depth, the dissolved δ^{13}C-CH_4 will vary based on initial bubble size. For example, at an altitude of 407.5 m, dissolved values δ^{13}C-CH_4 of −49.86‰, −49.23‰, and −49.18‰ were predicted from initial bubble diameters of 0.6, 0.8, and 1.0 cm, respectively. Similarly, dissolved δ^{13}C-CH_4 may have a value of −50‰ at altitudes of 90, 150, and 335 m above the seafloor given an initial bubble diameter of 0.2, 0.3, and 0.5 cm, respectively.

At an altitude of 407.5 m, water parcels influenced more by smaller bubbles would be responsible for lighter dissolved δ^{13}C-CH_4 values while parcels impacted preferentially by larger bubbles would have heavier dissolved δ^{13}C-CH_4 values. Comparing sample measurements and TAMOC model calculations of dissolved δ^{13}C-CH_4 from dive H1406, it seems that bubbles with initial diameters of 0.5 cm or less did not reach an altitude of 406 m (Figure 5). However, even the largest bubbles with an initial diameter of 1.0 cm do not explain the heaviest dissolved δ^{13}C-CH_4 measurements from dive H1406, values which likely display the influence of CH_4 oxidation as described below. For example, the dissolved isotopic values produced by the largest bubbles, with initial diameters of 0.8, 0.9, and 1.0 cm, are all very similar at an altitude of 407.5 m above the seafloor (Figure 5). Increasing the initial bubble diameter size further to 1.5 cm, not shown, resulted in dissolved CH_4 isotopic values at 407.5-m altitude that were lighter (more negative) than the 1.0-cm diameter bubbles. This is due to the change in dissolution rate following the natural formation of a clathrate hydrate skin around the bubble. When a bubble enters the water column within the clathrate hydrate stability zone, a CH_4 hydrate skin begins to form, and once it encapsulates the bubble, the dissolution rate decreases. Formation of the clathrate hydrate skin is faster for smaller bubbles than for bigger bubbles; thus, the

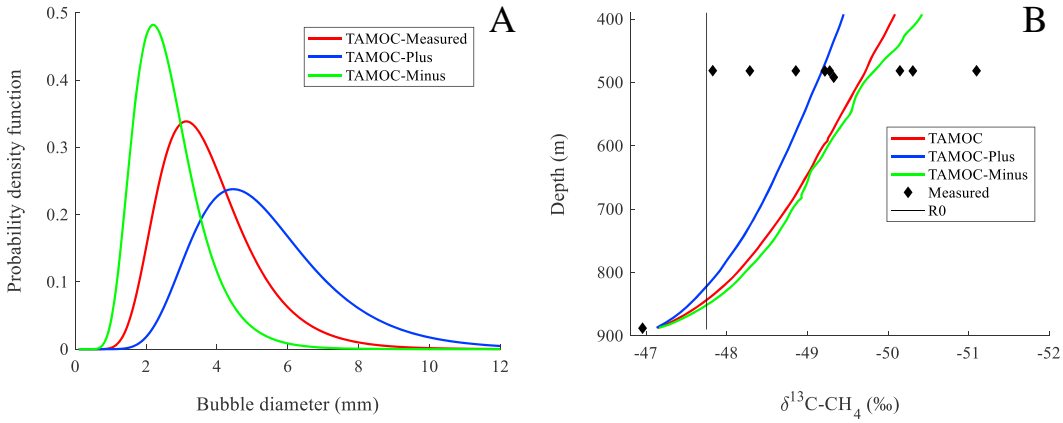

Figure 7. (a) Probability distribution function (PDF) of bubble sizes, for different TAMOC simulations. The red curve shows the PDF based on direct bubble size measurements. The blue curve shows the PDF generated by increasing the mean of the measured PDF by the standard deviation, while the green curve shows the PDF generated by decreasing the mean of the measured PDF by the standard deviation. (b) Plot of dissolved δ^{13}C-CH_4 against depth. Isotopic ratio distributions were calculated by considering the measured PDF of bubble sizes (red curve), a PDF shifted toward larger bubble sizes (blue curve), and a PDF shifted toward smaller bubble sizes (green curve). All three simulations were initialized based on gas bubble composition data collected on dive H1406. The solid black line shows the measured gas bubble δ^{13}C-CH_4 isotopic ratio, −47.75‰, from dive H1406 collected at the seafloor. The black diamonds show measured dissolved δ^{13}C-CH_4 from dive H1406. TAMOC = Texas A&M Oil spill (Outfall) Calculator.

clathrate hydrate skin encapsulates bigger bubbles at a higher altitude above the seafloor. The change in dissolution rate is apparent in most TAMOC model results (the kinks in each of the colored curves) and is easily identified in model runs using larger bubbles as a shift in the rate of change of δ^{13}C-CH_4 (Figure 5). Therefore, when we examine dissolved δ^{13}C-CH_4 values at any given depth, the bubbles with the largest initial diameter might not necessarily lead to the heaviest values of δ^{13}C-CH_4. The biggest bubbles would lose a larger fraction of CH_4 before clathrate hydrate skin formation, thus pushing the dissolved δ^{13}C-CH_4 toward lighter values.

4.3. TAMOC Model Sensitivity Analysis

Bubble size is an important factor controlling the fraction of CH_4 dissolved and the δ^{13}C-CH_4 dissolved in relation to altitude above the seafloor. As bubbles ascend, the fraction of CH_4 dissolved increases more quickly and δ^{13}C-CH_4 of dissolved CH_4 becomes lighter at a faster rate for smaller bubbles than for larger ones. In section 4.2 we modeled the dissolution of bubbles of specific sizes, but it is also important to consider changes in dissolution as the entire bubble size distribution shifts toward larger or smaller bubbles. Measurements of bubble size resulted in a lognormal distribution with a mean and standard deviation of 1.267 and 0.3532 mm, respectively, which translates to an arithmetic mean and standard deviation of 3.78 and 1.38 mm, respectively. In order to simulate a shift in the bubble size distribution, the lognormal mean of the original bubble size distribution was either increased or decreased by the lognormal standard deviation. This resulted in bubble size distributions with arithmetic means of 5.38 and 2.65 mm. Figure 7 shows the probability distribution functions (PDFs) for the different simulations along with the evolution of dissolved δ^{13}C-CH_4 as a function of depth. These simulations assumed an initial gas bubble composition based on gas bubble measurements collected on dive H1406, including a gas bubble δ^{13}C-CH_4 of −47.75‰. The different simulations are consistent with model results of different bubble sizes: a PDF shifted toward smaller bubble sizes results in lighter dissolved δ^{13}C-CH_4. The TAMOC simulations with different PDFs produced similar dissolved δ^{13}C-CH_4 at the seafloor which diverged as bubbles ascended through the water column. At an altitude of 406 m above the seafloor, dissolved δ^{13}C-CH_4 values calculated by the TAMOC model were within the range of measured values. Dissolved δ^{13}C-CH_4 values calculated by the TAMOC simulations with altered PDFs differed by 0.65‰, while measurements at 406-m altitude had a range of 3.27‰. This suggests that the spatial variability of the gas bubble flare through the water column has a greater potential to influence the divergence of dissolved δ^{13}C-CH_4 than changes to the bubble size distribution at the seafloor. As the natural bubble size distribution shifts toward larger or smaller bubbles, we expect the variability of dissolved

δ^{13}C-CH_4 in the water column to remain largely the same, while the average dissolved δ^{13}C-CH_4 isotopic ratio at any given depth would shift slightly toward lighter or heavier values.

4.4. Methane Oxidation

Taking bubble size into consideration can help explain the spread in dissolved δ^{13}C-CH_4 measurements at any given depth; however, different bubble sizes do not account for the heaviest measurements of dissolved δ^{13}C-CH_4 (Figure 5). Although a larger bubble may produce heavier dissolved δ^{13}C-CH_4 values than a smaller bubble at the same depth, as mentioned in section 4.2, there is a limit to this relationship. It is therefore possible that additional processes are influencing the isotopic ratios of dissolved CH_4, most likely microbial oxidation. This is because microbial oxidation of CH_4 has been shown to fractionate dissolved δ^{13}C-CH_4 toward heavier values, through the preferential uptake of the lighter carbon isotope, $^{12}CH_4$, which leaves the residual CH_4 pool enriched in $^{13}CH_4$ (e.g., Barker & Fritz, 1981; Leonte et al., 2017). This process would make dissolved δ^{13}C-CH_4 heavier than would be expected from dissolution alone.

We estimate the fraction of CH_4 consumed through oxidation by comparing the expected δ^{13}C-CH_4 of dissolved CH_4 calculated using the TAMOC model and measured dissolved δ^{13}C-CH_4. For this calculation we use a closed-system Rayleigh model (equation (4)), as was done previously (Leonte et al., 2017). This isotope model calculates the fraction of CH_4 removed (f_o) from the water column due to microbial oxidation. This model equation is more appropriate than the Instantaneous Product Rayleigh Model (equation (2)) described above, since the starting reactant for microbial oxidation is dissolved CH_4, which does not rapidly rise through the water column like a gas bubble.

$$f_o = 1 - \left[\frac{(\delta X + 1,000)}{(\delta D_0 + 1,000)}\right]^{\alpha_o/(1-\alpha_o)} \tag{4}$$

Using equation (4), we can calculate the fraction of dissolved CH_4 that has been oxidized, f_o, following dissolution at any given depth by considering the expected dissolved δ^{13}C-CH_4 calculated using the TAMOC model, δD_0, the measured dissolved δ^{13}C-CH_4, δX, and the fractionation factor due to microbial oxidation, α_o. For this calculation, we used a fractionation factor of α_o = 1.0115, based on the results of Leonte et al. (2017). Since the fractionation factor for oxidation is greater than that for dissolution, a relatively small fraction of CH_4 oxidized would correspond to a large shift in δ^{13}C-CH_4. Given the fractionation factor of α_o = 1.0115, an increase in dissolved δ^{13}C-CH_4 of 1‰ corresponds roughly to a f_o value of 0.1. At 407.5-m altitude, the TAMOC model predicted a dissolved δ^{13}C-CH_4 of −49.72‰ for dive H1406. Calculating f_o for measurements made from dive H1406 that were heavier than −49.72‰ resulted in values from 0.04 to 0.16. However, there is no reason that only the measurements with particularly heavy dissolved δ^{13}C-CH_4 values were affected by oxidation. The average measured dissolved δ^{13}C-CH_4 value from dive H1406 collected at 406 m above the seafloor was −49.37‰, corresponding to a value of f_o equal to 0.03. Although microbial oxidation helps to explain our measured values of dissolved δ^{13}C-CH_4, the relatively small f_o values calculated suggest that oxidation is removing only a small part of the dissolved CH_4 pool inside the rising bubble flare.

Considering the residence time of water in our study area is also important in quantifying the relative magnitude of CH_4 oxidation. The horizontal transect length at 400-m altitude during dive H1406 was 174 m. During the time samples were collected, the average water current velocity at that depth was 5.6 cm/s, making the residence time of water 0.9 hr. Microbial oxidation is expected to be active in this environment (Crespo-Medina et al., 2014; Du & Kessler, 2012; Kessler et al., 2011), yet the short residence time of water limits the extent of CH_4 oxidation between the time CH_4 dissolves into the water column and the time waters exit the study area. However, that does not mean that microbial oxidation did not remove significant CH_4 downcurrent, merely that our ability to observe its effects was limited in the narrow space of the bubble flare. The average fraction of CH_4 oxidized was calculated for dive H1406 to be 0.03. Given the average CH_4 concentration at 406-m altitude, 575 nM, and a residence time of 0.9 hr, the fraction oxidized is thus equivalent to a CH_4 oxidation rate of 395 nM/day. This estimate is among some of the fastest CH_4 oxidation rates measured to date (Leonte et al., 2017; Mau et al., 2013).

5. Conclusions

Measurements of $\delta^{13}C$-CH_4 over the Woolsey Mound gas seep in the northern Gulf of Mexico were used to reveal the dissolution dynamics of a CH_4 bubble flare. Differences in isotopic values between CH_4 in the gas and dissolved phase show that dissolution is occurring quickly following seafloor emission of gas bubbles and throughout the water column. The fraction of CH_4 dissolved at the seafloor ranges from 0.264 to 0.990 with an average of 0.582 based on calculations using the Instantaneous Product Rayleigh Isotope Model. Furthermore, the shift in dissolved $\delta^{13}C$-CH_4 toward lighter values higher in the water column is consistent with laboratory experiments that measured the fractionation of CH_4 isotopes during dissolution. Isotopic fractionation was added into the TAMOC model and produced similar results to the measurements as well as the independently determined Instantaneous Product Rayleigh Model. In addition, the TAMOC model showed that most of the spread in measured values of dissolved $\delta^{13}C$-CH_4 can be explained by the spatially heterogeneous distribution of bubble sizes. For example, water parcels impacted by a larger proportion of smaller bubbles resulted in lighter values of dissolved $\delta^{13}C$-CH_4. However, increasing the starting bubble diameter does not necessarily explain the heaviest values of dissolved $\delta^{13}C$-CH_4 measured. For these samples, microbial oxidation of dissolved CH_4 was necessary to explain these heavy isotope values. Yet despite rapid oxidation rates for samples collected inside the rising bubble flare, microbial oxidation played a limited role in removing dissolved CH_4 due to the relatively small spatial area of the bubble flare.

Acknowledgments

This research was made possible by two grants from the Gulf of Mexico Research Initiative: Gulf Integrated Spill Response (GISR) Consortium (awarded to J. D. K. and S. A. S.) and Center for Integrated Modeling and Assessment of the Gulf Ecosystem (C-IMAGE) II (awarded to S. A. S.). Additional support was provided by the U.S. Department of Energy (DE-FE0028980; awarded to J. D. K.). Data are publicly available through the Gulf of Mexico Research Initiative Information & Data Cooperative (GRIIDC). Methane concentration and isotopic ratio data can be found at https://data.gulfresearchinitiative.org/data/R1.x137.000:0025, and TAMOC model scripts and results are found at https://data.gulfresearchinitiative.org/data/R1.x137.000:0026. The coversion of methane isotopic ratio data used in this manuscript can be found at https://data.gulfresearchinitiative.org/data/R1.x137.000:0028. We want to thank the captain and crew of the E/V *Nautilus* and the operators of ROV *Hercules* and *Argus* during the GISR G08 cruise and Nicole Raineault for their outstanding support at sea. Acoustically identifying the bubble flare was managed by Andone Lavery, and support for collecting gas and water samples was provided by John Bailey. We also want to thank Sean Sylva for analytical assistance on shore, Inok Jun for helping create the sampling schematics, and David Brink-Roby for helping create the sample site map.

References

Bacsik, Z., Lopes, J. N. C., Gomes, M. F. C., Jancso, G., Mink, J., & Padua, A. A. H. (2002). Solubility isotope effects in aqueous solutions of methane. *Journal of Chemical Physics*, *116*(24), 10,816–10,824. https://doi.org/10.1063/1.1480012

Barker, J. F., & Fritz, P. (1981). Carbon isotope fractionation during microbial methane oxidation. *Nature*, *293*(5830), 289–291. https://doi.org/10.1038/293289a0

Ben-Naim, A., & Yaacobi, M. (1974). Effects of solutes on the strength of hydrophobic interaction and its temperature dependence. *Journal of Physical Chemistry*, *78*(2), 170–175. https://doi.org/10.1021/j100595a600

Breier, J. A., Sheik, C. S., Gomez-Ibanez, D., Sayre-McCord, R. T., Sanger, R., Rauch, C., Coleman, M., et al. (2014). A large volume particulate and water multi-sampler with in situ preservation for microbial and biogeochemical studies. *Deep-Sea Research Part I: Oceanographic Research Papers*, *94*, 195–206. https://doi.org/10.1016/j.dsr.2014.08.008

Brooks, J.M. (1975). Sources, sinks, concentrations, and sub-lethal effect of light aliphatic and aromatic hydrocarbons in the Gulf of Mexico, (Doctoral dissertation). Retrieved from [http://hdl.handle.net/1969.3/22656]. College Station, TX: Texas A&M Univ.

Ciais, P., Sabine, C., Bala, G., Bopp, L., Brovkin, V., Canadell, J., Chhabra, A., et al. (2013). Carbon and other biogeochemical cycles. In T. F. Stocker, et al. (Eds.), *Climate change 2013: The physical science basis. Contribution of working group I to the fifth assessment report of the intergovernmental panel on climate change*, (pp. 465–570). Cambridge Univ. Press: Cambridge, United Kingdom and New York. https://doi.org/10.1017/CBO9781107415324.015

Clift, R., Grace, J. R., & Weber, M. E. (1978). *Bubbles, drops, and particles*. New York; London: Academic Press.

Crespo-Medina, M., Meile, C. D., Hunter, K. S., Diercks, A.-R., Asper, V. L., Orphan, V. J., Tavormina, P. L., et al. (2014). The rise and fall of methanotrophy following a deepwater oil-well blowout. *Nature Geoscience*, *7*(6), 423–427. https://doi.org/10.1038/NGEO2156

Dansgaard, W. (1964). Stable isotopes in precipitation. *Tellus*, *16*(4), 436–468. https://doi.org/10.3402/tellusa.v16i4.8993

Du, M., & Kessler, J. D. (2012). Assessment of the spatial and temporal variability of bulk hydrocarbon respiration following the deepwater horizon oil spill. *Environmental Science & Technology*, *46*(19), 10,499–10,507. https://doi.org/10.1021/es301363k

Garcia-Tigreros Kodovska, F., Sparrow, K. J., Yvon-Lewis, S. A., Paytan, A., Dimova, N. T., Lecher, A., & Kessler, J. D. (2016). Dissolved methane and carbon dioxide fluxes in Subarctic and Arctic regions: Assessing measurement techniques and spatial gradients. *Earth and Planetary Science Letters*, *436*, 43–55. https://doi.org/10.1016/j.epsl.2015.12.002

Gros, J., Reddy, C. M., Nelson, R. K., Socolofsky, S. A., & Arey, J. S. (2016). Simulating gas-liquid-water partitioning and fluid properties of petroleum under pressure: Implications for deep-sea blowouts. *Environmental Science and Technology*, *50*(14), 7397–7408. https://doi.org/10.1021/acs.est.5b04617

Gros, J., Socolofsky, S. A., Dissanayake, A. L., Jun, I., Zhao, L., Boufadel, M. C., Reddy, C. M., et al. (2017). Petroleum dynamics in the sea and influence of subsea dispersant injection during *Deepwater Horizon*. *Proceedings of the National Academy of Sciences of the United States of America*, *114*(38), 10,065–10,070. https://doi.org/10.1073/pnas.1612518114

Harting, P., Schütze, H., & Christoph, G. (1976). Der thermodynamische Kohlenstoffisotopieeffekt im system CH4–H2O. *Isotopenpraxis Isotopes in Environmental and Health Studies*, *12*(6), 232–234. https://doi.org/10.1080/10256017608543923

Hoefs, J. (1997). Stable isotope geochemistry. *Earth and Environmental Science*, *9*(4), 388. https://doi.org/10.1016/0012-8252(73)90028-7

Hu, L., Yvon-Lewis, S. A., Kessler, J. D., & MacDonald, I. R. (2012). Methane fluxes to the atmosphere from deepwater hydrocarbon seeps in the northern Gulf of Mexico. *Journal of Geophysical Research*, *117*, C01009. https://doi.org/10.1029/2011JC007208

Jancsó, G. (2002). Interpretation of isotope effects on the solubility of gases. *Nukleonika*, *243*(3), 328–342. https://doi.org/10.1016/j.jtbi.2006.06.022

Johnson, J. E. (1999). Evaluation of a seawater equilibrator for shipboard analysis of dissolved oceanic trace gases. *Analytica Chimica Acta*, *395*(1-2), 119–132. https://doi.org/10.1016/S0003-2670(99)00361-X

Kessler, J. D., & Leonte, M. (2018). Concentrations of gas dissolved in seawater and in gas bubbles collected in the northern Gulf of Mexico, April 12-20, 2015. Distributed by Gulf of Mexico Research Initiative Information and Data Cooperative (GRIIDC). Corpus Christi, TX: Harte Res. Inst., Texas A&M Univ., doi:https://doi.org/10.7266/N7610XXW

Kessler, J. D., Valentine, D. L., Redmond, M. C., Du, M., Chan, E. W., Mendes, S. D., Quiroz, E. W., et al. (2011). A persistent oxygen anomaly reveals the fate of spilled methane in the deep Gulf of Mexico. *Science*, *331*(6015), 312–315. https://doi.org/10.1126/science.1199697

Knox, M., Quay, P. D., & Wilbur, D. (1992). Kinetic isotopic fractionation during air-water gas transfer of O_2, N_2, CH_4, and H_2. *Journal of Geophysical Research*, *97*(C12), 20,335–20,343. https://doi.org/10.1029/92JC00949

Lapham, L. L., Wilson, R. M., & Chanton, J. P. (2012). Pressurized laboratory experiments show no stable carbon isotope fractionation of methane during gas hydrate dissolution and dissociation. *Rapid Communications in Mass Spectrometry*, *26*(1), 32–36. https://doi.org/10.1002/rcm.5290

Leonte, M., & Kessler, J. D. (2018). Mathematical conversion of δ^{13}C-CH_4 for methane dissolved in water using raw data collected in the northern Gulf of Mexico, April 12-20, 2015. Distributed by Gulf of Mexico Research Initiative Information and Data Cooperative (GRIIDC). Corpus Christi, TX: Harte Research Institute, Texas A&M University. https://doi.org/10.7266/n7-g26b-a359

Leonte, M., Kessler, J. D., Kellermann, M. Y., Arrington, E. C., Valentine, D. L., & Sylva, S. P. (2017). Rapid rates of aerobic methane oxidation at the feather edge of gas hydrate stability in the waters of Hudson Canyon, US Atlantic Margin. *Geochimica et Cosmochimica Acta*, *204*, 375–387. https://doi.org/10.1016/j.gca.2017.01.009

Macelloni, L., Brunner, C. A., Caruso, S., Lutken, C. B., D'Emidio, M., & Lapham, L. L. (2013). Spatial distribution of seafloor bio-geological and geochemical processes as proxies of fluid flux regime and evolution of a carbonate/hydrates mound, northern Gulf of Mexico. *Deep-Sea Research Part I: Oceanographic Research Papers*, *74*, 25–38. https://doi.org/10.1016/j.dsr.2012.12.006

Macelloni, L., Lutken, C. B., Ingrassia, M., D' Emidio, M., & Pizzi, M. (2016). Mesoscale biogeophysical characterization of Woolsey Mound (northern Gulf of Mexico), a new attribute of natural marine hydrocarbon seeps architecture. *Marine Geology*, *380*, 330–344. https://doi.org/10.1016/j.margeo.2016.03.016

Mau, S., Blees, J., Helmke, E., Niemann, H., & Damm, E. (2013). Different methanotrophic potentials in stratified polar fjord waters (Storfjorden, Spitsbergen) identified by using a combination of methane oxidation techniques. *Biogeosciences Discussions*, *10*(4), 6461–6491. https://doi.org/10.5194/bgd-10-6461-2013

Mau, S., Heintz, M. B., & Valentine, D. L. (2012). Quantification of CH4 loss and transport in dissolved plumes of the Santa Barbara Channel, California. *Continental Shelf Research*, *32*, 110–120. https://doi.org/10.1016/j.csr.2011.10.016

McGinnis, D. F., Greinert, J., Artemov, Y., Beaubien, S. E., & Wüest, A. (2006). Fate of rising methane bubbles in stratified waters: How much methane reaches the atmosphere? *Journal of Geophysical Research*, *111*, C09007. https://doi.org/10.1029/2005JC003183

Reeburgh, W. (2007). Oceanic methane biogeochemistry. *American Chemical Society*, *107*(2), 486–513. https://doi.org/10.1021/cr050362v

Rehder, G., Leifer, I., Brewer, P. G., Friederich, G., & Peltzer, E. T. (2009). Controls on methane bubble dissolution inside and outside the hydrate stability field from open ocean field experiments and numerical modeling. *Marine Chemistry*, *114*(1–2), 19–30. https://doi.org/10.1016/j.marchem.2009.03.004

Rice, P. A., Gale, R. P., & Barduhn, A. J. (1976). Solubility of butane in water and salt solutions at low temperatures. *Journal of Chemical and Engineering Data*, *21*(2), 204–206. https://doi.org/10.1021/je60069a021

Seewald, J. S., Doherty, K. W., Hammar, T. R., & Liberatore, S. P. (2002). A new gas-tight isobaric sampler for hydrothermal fluids. *Deep-Sea Research Part I: Oceanographic Research Papers*, *49*(1), 189–196. https://doi.org/10.1016/S0967-0637(01)00046-2

Solomon, E. A., Kastner, M., MacDonald, I. R., & Leifer, I. (2009). Considerable methane fluxes to the atmosphere from hydrocarbon seeps in the Gulf of Mexico. *Nature Geoscience*, *2*(8), 561–565. https://doi.org/10.1038/ngeo574

Umano, S., & Nakano, Y. (1958). Solubilities of propane and n-butane in water and common-salt solution. *Kogyo Kagaku Zasshi*, *61*(5), 536–542. https://doi.org/10.1246/nikkashi1898.61.536

Wang, B., & Socolofsky, S. A. (2015). A deep-sea, high-speed, stereoscopic imaging system for in situ measurement of natural seep bubble and droplet characteristics. *Deep-Sea Research Part I: Oceanographic Research Papers*, *104*, 134–148. https://doi.org/10.1016/j.dsr.2015.08.001

Wang, B., & Socolofsky, S. A. (2018), Simulation of the fates of natural gas seep bubbles with isotope ratio calculation at MC 118, Gulf of Mexico, April 17–18, 2015. Distributed by Gulf of Mexico Research Initiative Information and Data Cooperative (GRIIDC). Corpus Christi, TX: Harte Res. Inst., Texas A&M Univ. doi:https://doi.org/10.7266/N79K48TN

Wang, B., Socolofsky, S. A., Breier, J. A., & Seewald, J. S. (2016). Observations of bubbles in natural seep flares at MC 118 and GC 600 using in situ quantitative imaging. *Journal of Geophysical Research: Oceans*, *121*, 2203–2230. https://doi.org/10.1002/2015JC011452

Warzinski, R. P., Lynn, R., Haljasmaa, I., Leifer, I., Shaffer, F., Anderson, B. J., & Levine, J. S. (2014). Dynamic morphology of gas hydrate on a methane bubble in water: Observations and new insights for hydrate film models. *Geophysical Research Letters*, *41*, 6841–6847. https://doi.org/10.1002/2014GL061665

Weber, T. C., Mayer, L., Jerram, K., Beaudoin, J., Rzhanov, Y., & Lovalvo, D. (2014). Acoustic estimates of methane gas flux from the seabed in a 6000 km^2 region in the Northern Gulf of Mexico. *Geochemistry, Geophysics, Geosystems*, *15*, 1911–1925. https://doi.org/10.1002/2014gc005271

Wiesenburg, D. A., & Guinasso, N. L. Jr. (1979). Equilibrium solubilities of methane, carbon monoxide, and hydrogen in water and sea water. *Journal of Chemical & Engineering Data*, *24*(4), 356–360. https://doi.org/10.1021/je60083a006

Yvon-Lewis, S. A., Hu, L., & Kessler, J. D. (2011). Methane flux to the atmosphere from the deepwater horizon oil disaster. *Geophysical Research Letters*, *38*, L01602. https://doi.org/10.1029/2010GL045928